Planes of oxygen vacancies with a small band gap created in TiO_2 by application of electric field

Tyler C. Sterling,[1,*] Feng Ye,[2] Seohyeon Jo,[3] Anish Parulekar,[1]
Yu Zhang,[1] Gang Cao,[1,4] Rishi Raj,[5] and Dmitry Reznik[1,4,†]

[1]*Department of Physics, University of Colorado, Boulder, Colorado 80309, USA*
[2]*Neutron Scattering Division, Oak Ridge National Lab, Oak Ridge, Tennessee 37830, USA*
[3]*Materials Science and Engineering, University of Colorado, Boulder, Colorado 80309, USA*
[4]*Center for Experiments on Quantum Materials, University of Colorado, Boulder, Colorado 80309, USA*
[5]*Department of Mechanical Engineering, University of Colorado, Boulder, Colorado 80309, USA*

(Dated: April 9, 2024)

Our in-situ diffuse neutron scattering experiments have revealed that when electric current is passed through single crystals of rutile TiO_2 under conditions conducive to flash sintering, it induces the formation of parallel planes of oxygen vacancies. Specifically, a current perpendicular to the *c*-axis generates planes normal to the (132) reciprocal lattice vector, whereas currents aligned with the *c*-axis form planes normal to the (132) and to the (225) vector. This structural modification is linked to the appearance of signatures of interacting Ti^{3+} moments in magnetic susceptibility, signifying a structural collapse around the vacancy planes. Electrical conductivity measurements of the modified material reveal several electronic transitions between semiconducting states (via a metal-like intermediate state) with the smallest gap being 13.5 meV. Pristine TiO_2 can be restored by heating followed by slow cooling in air. Our work suggests a novel paradigm for achieving switching of electrical conductivity by applying an electric field.

I. INTRODUCTION

Flash sintering is a rapidly emerging technique focused on the processing of materials [1–5]. It involves the application of an electric field to dramatically reduce sintering time and temperature required to densify ceramic materials. Unlike traditional sintering methods that can take hours or even days, flash sintering can achieve similar or better results in a matter of seconds. This process not only conserves energy but also opens new pathways for the synthesis of materials or compositions with novel properties.

Here we applied an electric field to rutile TiO_2 single crystals under the conditions of flash sintering to rapidly modify the atomic structure and switch electrical resistivity from a high to a low resistance state. Our in-situ neutron diffuse scattering measurements have shown that this process consistently generates oriented parallel planes of structural defects, presumably oxygen vacancies, that are stable at room temperature. This variant of TiO_2 has a bandgap that is reduced from 3.4 eV in the pristine material to 13.5 meV. Furthermore magnetic susceptibility measurements have identified enhanced non-Curie-Weiss magnetic susceptibility consistent with occurrence of Ti^{3+} ions with interacting moments, hinting at a structural collapse around the planes of oxygen vacancies.

Our findings open a path towards engineering memrisor devices based on current-induced introduction of defects into TiO_2.

* ty.sterling@colorado.edu
† dmitry.reznik@colorado.edu

II. EXPERIMENTAL DETAILS

During flash [3] the sample is first held at an elevated temperature and an electric field (E-field) across the sample is applied (Fig. 1a). The E-field is increased continuously or stepwise until the resistivity starts to fall nonlinearly. In Fig. 1b this occures at 6 min. when the E-field reaches 150 V/cm. Eventually, (at 8 min) it switches abruptly by more that an order of magnitude to a low-resistance state and the power supply hits the current limit. At this point voltage is automatically regulated to maintain constant current, which signals the onset of flash. Alternatively, a constant E-field can be applied and temperature increased to a critical value where the resistivity drop occurs. Usually, the sample in this (flash) state glows brightly due to electroluminescence; however, sometimes the glowing isn't visible depending on the luminescence spectrum and brightness, which depend on material properties [7]. The sample stays in the flash state as long as the current is controlled under steady-state conditions. At this point the sample can be pulled out of the furnace and even submerged in liquid nitrogen (LN2) without interrupting flash. We show below that TiO_2 looses some oxygen during flash. Turning off the current and slowly cooling the sample in air leads to reabsorption of oxygen and the restoration of the pristine high-resistance state. Immersion of the flashing sample in LN2 followed by shut-off of the current quenches ("freezes in") the atomic structure created as a result of flash. The flash-modified state can also be preserved after the E-field is turned off if the sample is flashed in vacuum. This process varies somewhat from material to material; in some cases, flash occurs under moderate critical E-field strengths at room temperature.

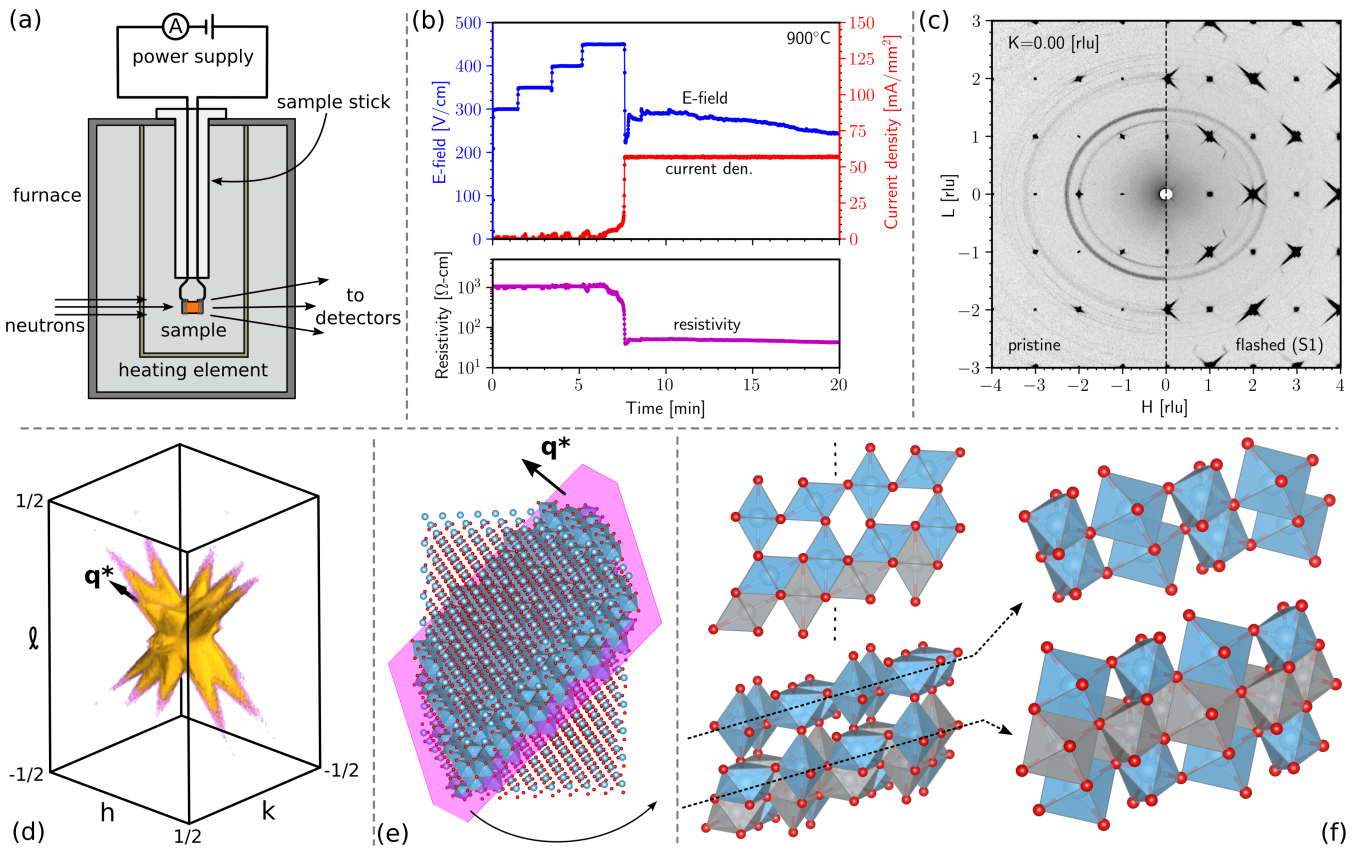

FIG. 1. (a) Schematic of the in-situ neutron scattering flash experiment during the constant-current conditions in the typical I-V curve during flash in (b). When the E-field is increased to a critical value, the resistivity drops sharply (∼ an order of magnitude); this occurs at about 7.5 minutes. (c) Scattering pattern from pristine (left) and flashed (right) samples in the H-L plane with $K = 0$. (d). Diffuse scattering features from the S1 dataset in (c) translated into the 1^{st} Brillouin zone and summed as discussed in the text. (e) A model of a Magnéli phase shear plane as described in ref. [6]. The vector $\boldsymbol{q}^*$ in (d) and (e) points along $(1\bar{3}2)$ and the displacement vector for the shear in (e) is 1/2[011]. (f) A model of the defect region in (e) showing different views (left) and an exploded view (right). The shear plane consists of chains of face-sharing octahedra (gray) separated by rutile-like edge sharing octahedra (blue). Between shear planes, the structure is rutile.

In order to understand structural modifications of materials during flash we designed, built, and commissioned an apparatus for in-situ neutron scattering measurements of samples under controlled E-field and high temperatures at the CORELLI diffractometer at the Spallation Neutron Source (SNS) at the Oak Ridge National Laboratory. The instrument combines the high efficiency of white beam Laue diffraction with energy discrimination for measuring both elastic scattering and total scattering in a single experiment over large volumes of reciprocal space. It also can access large momentum transfer $\boldsymbol{Q}$ and high momentum resolution to distinguish the diffuse signal from nearby Bragg peaks [8].

Elastic neutron scattering experiments were performed on rutile TiO_2 single crystals with current along b- and c-axes. For current along b, we measured a crystal in-situ and a pre-flashed one ex-situ. The latter was quenched in LN2 after flashed in air. The in-situ experiments were conducted at multiple temperatures and current densities to study the dependence of the scattering on flash conditions. For current along the c-direction, we measured one sample and one current density. A separate measurement was also conducted on the c-axis flashed sample ex-situ to characterize the structural modifications using low-background close cycle refrigerator. In this work, we mainly focus on two samples: sample-1 (S1) which was flashed in *air* with current along the b-axis and then quenched and sample-2 (S2), which was flashed in *vacuum* (i.e. in the furnace at the SNS) with current along the c-axis. Dimension of all samples that we measured were $10 \times 3 \times 1$ mm.

Temperature-dependence of electrical resistivity and magnetic susceptibility were measured on a pristine single crystal and on S2 using the Quantum Design MPMS system. S1 broke during the neutron scattering experiments and the resulting pieces were too small for reliable transport measurements. The conductivity of the pristine sample was too small to measure, and the flashed sample was too thin to measure conductivity in the ab plane.

III. RESULTS

The results of the in-situ neutron scattering measurements with electrical current passing through the sample were qualitatively similar to the results on the ex-situ flashed samples, with a notable difference for S2. Fig. 1 shows that the primary effect of flash is that Bragg peaks acquire needle-like shoulders, which extend in all symmetry equivalent (132) directions. In what follows, we use Miller indices in the basis of primitive rutile lattice vectors (tetragonal symmetry with $a = b \neq c$).

The same (132) features are present in both S1 and S2. However, in S2, we also note the occurrence of less pronounced needles oriented along (225) [fig. 2b]. The difference in the apparent widths of features in fig. 2 a) vs b) is due to instrument resolution: the two samples were mounted with different orientations in the scattering plane.

Intensity and asymmetry of the needles vary from Bragg peak to Bragg peak due to structure factor effects. It is useful to project all diffuse scattering features into the first Brillouin zone, where a sea urchin-like pattern is evident. We picked all Brillouin zones in each data set with significant diffuse scattering, translated them to the 1^{st} Brillouin zone, then summed them (see fig. 2 and supp. info [9]).

We determined directions of the needles by fitting the coordinates of the intersection of the needles with integrated planes of intensity cut through the summed data. The needle directions are all equivalent under tetragonal symmetry operations: the reported direction for each data set is determined by averaging the fits over all steps and over all needles for each data set. We call different symmetry-equivalent needles k_1, k_2, ..., h_1, ..., etc [9]. In fig. 3, we show current and temperature dependent cuts along several different needles. These cuts are made along straight lines in reciprocal space that do not follow high symmetry directions, but rather align with the needle orientations. Since the needle orientations are away from high-symmetry directions, we present data in Å^{-1}. See the supp. info for details of fitting the needle directions and for additional cuts along needles [9].

It is well-known that needle-like structures in diffraction correspond to planar correlation in real space. We can understand that the primary effect of flash on TiO_2 is to produce either pancake-like clusters of defects and/or slip dislocations oriented perpendicular to the needles. Fitting the S1 dataset, where we have the most comprehensive data, allowed us to estimate the correlation lengths of the defects to be about 46 Å perpendicular to the pancake planes and ~ 200 Å in the planes (line cuts perpendicular to the needles are resolution-limited: see supp. info [9]).

Fig. 3 compares the scattering intensity distribution for representative cuts along the needles of the in-situ S1 sample at different electrical current densities and temperatures. (Note that during flash the sample temperature is higher due to heating by electric current. Experiments to quantitatively characterize this heating are planned.) Background subtracted from the data was obtained by taking cuts through the nearby intensity where no diffuse scattering was present. There is no diffuse scattering from the pristine sample: Only resolution-limited Bragg peaks are present. Diffuse scattering tails of the Bragg peaks are clearly visible in the flashed samples. Although the needle orientation does not depend on current, the diffuse intensity increases with increasing current density. The dependence on the current is not linear – 40mA at 100C produced less diffuse intensity than higher currents where the effect seems to saturate. Interestingly, the largest diffuse intensity originates from the quenched sample.

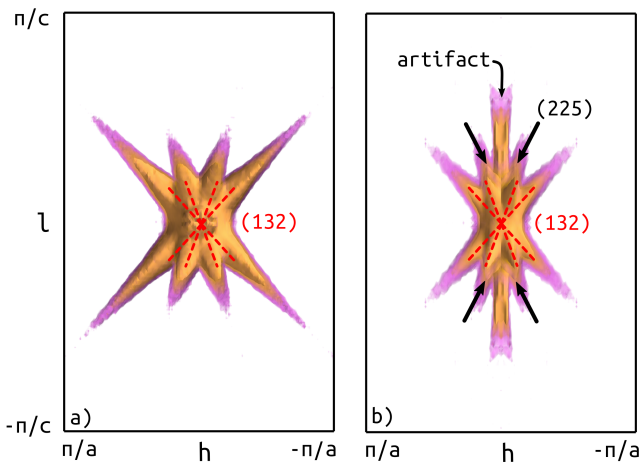

FIG. 2. Volumetric plots of the summed S1 (a) and S2 (b) datasets. The dashed green lines label the (132) features, whereas black arrows label the (225) features. (a) Sample was flashed and quenched in air and the current was perpendicular to the b-axis. (b) The sample was flashed in vacuum and then was allowed to cool. Current was parallel to the c-axis. The artifact labeled in (b) is from neutrons saturating the detectors; it is not physically interesting.

The temperature dependence of the electrical conductivity of S2 (fig. 4b) at low temperature $T \lesssim 50$ K is well described by the semiconductor formula $\sigma(T) = \sigma_0 \exp(-E_A/k_B T)$ with $E_A = 13.5$ meV and $\sigma_0 = 39.7$ $(\text{Ohm-cm})^{-1}$. In the high temperature regime, $T \gtrsim 150$ K, $E_A = 15.2$ meV and $\sigma_0 = 2.5$ $(\text{Ohm-cm})^{-1}$, though the fit isn't as good. An alternative procedure would be to assume multiple gaps in the high temperature regime [10, 11].

In the intermediate temperature regime, 60 K $\gtrsim T \lesssim$ 150 K, the temperature dependence is fit as $\sigma(T) = 1/[\rho_D + \rho_0(T/\Theta)^n]$, consistent with a metal. ρ_D is the resistivity due to defect scattering, ρ_0 the characteristic resistivity from all other forms of scattering, (Θ) the temperature scale, and n the exponent: at low enough temperature, $n = 5$ corresponds to electron-phonon scattering and $n = 2$ to electron-electron scattering. Often, for small changes in T, $n = 1$ is also used as an empir-

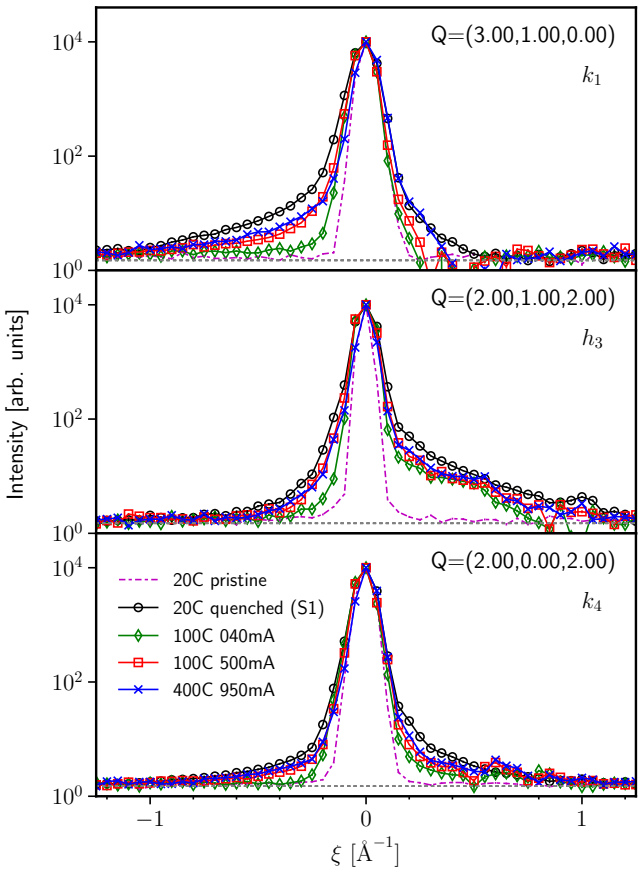

FIG. 3. Current and temperature dependence of the diffuse scattering features along different needles thru different Bragg peaks labeled in the figures. Background due to the furnace and electrodes was subtracted. Since the needles aren't oriented along a high-symmetry direction, we plot data in Å^{-1}. See the text and supp. info [9] for detailed explanation of the coordinates and orientation of the needles.

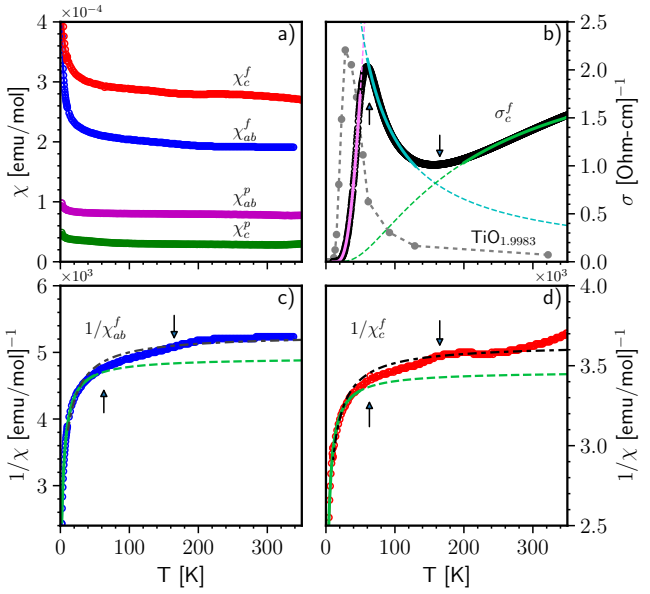

FIG. 4. Magnetic susceptibility χ (a), electrical conductivity σ (b), and $1/\chi$ (c-d) of pristine and flashed S2 sample (see text). χ^f_{ab} and χ^f_c are the susceptibilities in the ab plane and along the c-axis respectively. σ^f_c is the conductivity along the c-axis of the flashed sample. The arrow indicates the position of the 'dip' in the conductivity which coincides with anomalies in the susceptibility. The different curves plotted with σ and $1/\chi$ corresponds to fits through different temperature regimes as discussed in the text. The gray markers in b) are conductivity data for TiO$_{1.9983}$ from ref. [10] divided by 10.

ical estimate. We fit ρ_D, ρ_0, and n. We find $\rho_D \approx 0$ (Ohm-cm) an $n \approx 1$, so that $\sigma(T) \sim \sigma_0 \times (\Theta/T)$ with $\sigma_0 = 1/\rho_0 = 0.2$ (Ohm-cm)$^{-1}$ and $\Theta = 654.5$ K. It is interesting to note that Θ is similar to but lower than the known Debye temperature of pristine rutile TiO_2, $\Theta_D =$ 943 K [12], though the interpretation with $n \equiv 1$ isn't physically meaningful. Moreover, our fit suggests that defect scattering (ρ_D) is significant as expected from a large concentration of defects established above.

The magnetic susceptibilities were fit assuming Curie-Weiss behavior to extract magnetic moments, $\mu_{eff} = \sqrt{8C}$, and Curie-Weiss temperatures, Θ_{CW}. We also included a temperature independent contribution , χ_0, to the susceptibility. Explicitly, we assume $\chi(T) = \chi_0 + C/(T - \Theta_{CW})$. Above about 60 K, the susceptibilities of the flashed sample deviated significantly from Curie-Weiss behavior (figs. 4 c-d). We fit both the Curie-Weiss like low temperature regimes (dashed lines in figs. 4 c and d) and the full curves (dashed-dotted lines in figs. 4 c-d) separately. Only the parameters extracted from the low-T regime for the flashed samples are physically sensible and we focus on these here. Fits to the full temperature range are provided in the supp. info. [9]. The pristine samples were Curie-Weiss like all the way up to $T \sim$300 K.

At low temperature, we find $\mu_{eff} = 0.024\ \mu_B$/Ti in the ab plane of the pristine sample and $\mu_{eff} = 0.025\ \mu_B$/Ti along the c-axis of the pristine sample. For the flashed sample, $\mu_{eff} = 0.069\ \mu_B$/Ti in the ab plane and $\mu_{eff} = 0.065\ \mu_B$/Ti along the c-axis. The increase in the effective moment in S2 is consistent with the emergence of $Ti^{3+}(3d^1)$ ions. χ_0 and Θ_{cw} are provided in the supp. info. [9].

Both susceptibilities of the flashed sample show anomalies at $T \approx 165$ K (down-arrows in figs. 4b-d). Along the c-axis, there is a dip in the susceptibility; in the ab plane, there is a "kink". There are no corresponding anomalies in the susceptibilities of the pristine sample. It is intriguing that there is minimum in the conductivity at the same T (fig. 4b). There is also a maximum in the conductivity at $T \approx 60$ K (up-arrow in fig. 4b); $T \approx 60$ K is where the susceptibilities of the flashed sample begin to deviate significantly from Curie-Weiss behavior (up-arrows in figs. 4c-d).

IV. DISCUSSION AND CONCLUSIONS

Flash/quench treatment leads to radical yet reproducible, and therefore potentially controlled, modifications of atomic structure and bulk properties. Here we demonstrated that planar defects are introduced into TiO_2 switching it to a low resitance phase. Insulators, such as Yttria-stabilized zirconia, often become metallic. In the quasi-2D quantum material Pr_2CuO_4, this treatment enhances oxygen vacancy ordering, which in turn increases the three-dimensionality of electrical resistivity and magnetization, and sharpens Raman-active phonons. [7].

Although the atomistic mechanism of flash is still enigmatic, it has been successfully applied across a broad spectrum of materials, from metals like aluminum [13, 14] and tungsten [14] to both simple and complex oxides [2]. Typically, ceramics that would need hours at approximately ∼1500°C to sinter can now be consolidated from powders in just seconds at temperatures significantly below 1000°C under flash conditions. Recent advancements in flash sintering include the synthesis of new materials, such as high-entropy oxides with potential for exceptional lithium-ion conductivity in next-generation batteries [15], and the transformation of insulators into metals. Flash was initially observed in polycrystalline materials where it was attributed to Joule heating at grain boundaries [16], but its discovery in single crystals [17] revealed that it is a bulk effect.

Rutile TiO_2, a wide-gap insulator transparent to visible light, becomes electrically conducting and light-absorbing when slightly reduced to TiO_{2-x} ($x < 2$) [11, 18, 19]. This change is due to the formation of Magnéli phases, where oxygen vacancies aggregate into semiconducting planes, causing a shear dislocation of adjacent rutile slabs [6, 18, 20–23]. The chemical formulae of the Magnéli phases are Ti_nO_{2n-1}. The orientation and density of these defect planes depends on n. For commonly studied more-reduced phases, $4 \leq n \leq 10$, the shear planes are perpendicular to (121) [22, 24]. For slightly-reduced phases, $15 \leq n \leq 39$, the shear planes are perpendicular to (132) [18, 20, 25, 26] and the displacement vector of the shear between adjacent rutile slabs is $1/2\langle 0\bar{1}1\rangle$ [11, 21]. In these phases, the two-dimensional character of the conducting planes containing Ti $3d$ electrons has the potential to host novel electronic properties [27–31].

During flash, it is possible that oxygen vacancies already present in the samples order as a result of the E-field; More likely though oxygen vacancies form in the material with the excess oxygen diffusing out of the sample.

Our observations of needle-like structures forming along the (132) and equivalent crystallographic directions in both in-situ and quenched samples, indicate the formation of the (132) Magnéli phase. This structure is notoriously difficult to synthesize via conventional annealing, leaving many of its properties unexplored until now [10, 11, 19]. Our research aims to bridge this knowledge gap. We have found the formation of the (132) phase to be remarkably consistent, evident in both S1 and S2 samples despite their preparation under varying conditions (flashed in air vs. vacuum, current along b vs c) and across a wide range of temperatures and current densities. In particular, the (132) scattering emerges as a dominant feature in the S2 sample, though the presence of subtler needle-like patterns along (225) also warrants mention. The relationship of this (225) feature to the current direction or the vacuum environment in S2 remains an open question. Our ongoing research seeks to clarify the impact of these variables. Furthermore, we acknowledge the prior identification of disordered (101), (100), and (725) features in slightly reduced rutile [10, 18], highlighting that while other defects do form, the (121) and (132) phases are the most pronounced.

Previous efforts to synthesize Magnéli phases through annealing required extensive time periods, tens of hours or more at around 1000°C, to achieve homogeneously reduced samples [10, 11, 19]. In contrast, our research demonstrates that the (132) phase can be rapidly produced in bulk crystals in just minutes at significantly reduced temperatures, approximately 400°C, using flash sintering. This result prompts an intriguing question if the (121) phase could also be synthesized in single crystals exhibiting greater oxygen deficiency through flash sintering? The successful creation of this phase under such conditions has indeed been documented in ceramic TiO_2 [32].

Comparing our findings with earlier research on slightly reduced rutile, which featured lower oxygen vacancy concentrations ($0.00001 < x < 0.0001$) [10, 11], provides valuable insights. In these cases, shear planes were either absent or scarcely formed, with electrical transport primarily occurring through hopping between isolated Ti interstitials dispersed throughout the material. The emergence of a few shear planes at higher vacancy concentrations was found to impede hopping, leading to reduced conductivity. However, the pronounced scattering intensity related to the (132) shear planes in our neutron diffuse scattering data indicates a substantially higher x in our samples, signifying a greater concentration of oxygen vacancies. Previous studies estimated activation energies to be around ~ 1 meV and reported conductivity an order of magnitude higher than that observed in our samples, which possess notably larger oxygen vacancy concentrations. This discrepancy likely stems from the distinct nature of transport mechanisms: in earlier studies, shear planes primarily served to scatter carriers, whereas in our samples, transport appears to be predominantly confined within the planes themselves, akin to behavior seen in more significantly reduced Magnéli phases, such as Ti_4O_7 [31].

Finally, we explore the promising application of the electric field-induced switchability of TiO_2 for memristor technology, where the binary states of memory bits are represented by low and high resistance levels. We

have demonstrated that TiO_2 can transition from a high-resistance to a low-resistance state through the application of electric current (Fig. 1b), a change attributed to the formation of oxygen defect planes. When scaled down and embedded within a device, we anticipate a similar switchability, albeit with notable distinctions. Crucially, TiO_2 reabsorbs oxygen when cooled slowly post-flash, implying that either rapid quenching or conducting the flash process in a vacuum is essential to maintain the low-resistance state. Yet, in a device setting, rapid cooling upon deactivation of the electric field is expected due to efficient thermal dissipation to the substrate, potentially enabling an "always quenched" mode where TiO_2 solidifies before oxygen reintegration. In this context it is important to highlight that the diffuse intensity is higher for the quenched samples (S1) (Fig. 3), i.e. the effect is more pronounced when the sample is quenched. This phenomenon suggests that understanding the mechanisms behind this unusual scattering behavior could provide valuable insights into optimizing the performance and stability of memristive devices. Essentially, we have outlined a method to toggle TiO_2 between resistive states via electric field application. Future research will be required to devise a technique for reoxidizing TiO_2 by applying an electric field in a novel configuration to reverse the switching process.

V. ACKNOWLEDGEMENT

Work at the University of Colorado was supported by U.S. Department of Energy, Office of Basic Energy Sciences, Office of Science, under Contract No. DE-SC0024117. Research at ORNL's SNS was sponsored by the Scientific User Facilities Division, Office of Basic Energy Sciences, U.S. Department of Energy (DOE). T.S. was supported by the U.S. Department of Energy, Office of Science, Office of Workforce Development for Teachers and Scientists, Office of Science Graduate Student Research (SCGSR) program. The SCGSR program is administered by the Oak Ridge Institute for Science and Education for the DOE under contract number DE-SC0014664. G.C. acknowledges NSF support via Grant No. DMR 2204811.

[1] D. Yadav, Y. Yuan, V. Gopalan, R. Raj, and S. Jo, Journal of the American Ceramic Society **106**, 46 (2023).
[2] R. Raj, A. Kulkarni, J.-M. Lebrun, and S. Jha, MRS Bulletin **46**, 36 (2021).
[3] R. Raj, Journal of the American Ceramic Society **99**, 3226 (2016).
[4] R. Raj, Journal of the European Ceramic Society **32**, 2293 (2012).
[5] M. Cologna, B. Rashkova, and R. Raj, Journal of the American Ceramic Society **93**, 3556 (2010).
[6] L. Bursill and B. Hyde, Acta Crystallographica Section B: Structural Crystallography and Crystal Chemistry **27**, 210 (1971).
[7] S. Roy, F. Ye, Z. Morgan, S. I. Jalali, Y. Zhang, G. Cao, N.-H. Kaneko, M. Greven, R. Raj, and D. Reznik, arXiv preprint arXiv:2302.04385 (2023).
[8] F. Ye, Y. Liu, R. Whitfield, R. Osborn, and S. Rosenkranz, Journal of applied crystallography **51**, 315 (2018).
[9] See Supplemental Material at [URL-will-be-inserted-by-publisher] for detailed descriptions of the methods used in this paper, results of numerical fitting of the neutron scattering data, as well as additional 1D, 2D, and 3D (volumetric) plots of the diffuse scattering data.
[10] R. R. Hasiguti and E. Yagi, Physical Review B **49**, 7251 (1994).
[11] E. Yagi, R. R. Hasiguti, and M. Aono, Physical Review B **54**, 7945 (1996).
[12] A. Wu and R. Sladek, Physical Review B **25**, 5230 (1982).
[13] B. McWilliams, J. Yu, and F. Kellogg, Journal of materials science **53**, 9297 (2018).
[14] R. Raj, private communication.
[15] N. Yan, Y. Zhu, M. Cai, B. Li, B. Xu, Y. Li, X. Wang, and Z. Jia, Materials **15**, 3836 (2022).
[16] M. Yu, S. Grasso, R. Mckinnon, T. Saunders, and M. J. Reece, Advances in Applied Ceramics **116**, 24 (2017).
[17] D. Yadav and R. Raj, Scripta Materialia **134**, 123 (2017).
[18] L. Bursill, B. Hyde, O. Terasaki, and D. Watanabe, Philosophical Magazine **20**, 347 (1969).
[19] R. Hasiguti, E. Yagi, and M. Aono, Radiation Effects **4**, 137 (1970).
[20] L. Bursill and B. Hyde, Philosophical Magazine **23**, 3 (1971).
[21] L. Bursill and B. Hyde, Proceedings of the Royal Society of London. A. Mathematical and Physical Sciences **320**, 147 (1970).
[22] Q. Zhang, W. Liu, Y. Zhou, J. Li, T. Sun, Q. Liu, Y. Ma, J. Wang, J. Li, R. Zhao, *et al.*, Zeitschrift für anorganische und allgemeine Chemie **647**, 126 (2021).
[23] L. Liborio and N. Harrison, Physical Review B **77**, 104104 (2008).
[24] S. Andersson, D. H. Templeton, S. Rundqvist, E. Varde, and G. Westin, Acta chem. scand **14**, 1161 (1960).
[25] C. Chu, Physical Review B **1**, 4700 (1970).
[26] E. Yagi and R. R. Hasiguti, Journal of the Physical Society of Japan **43**, 1998 (1977).
[27] M. Taguchi, A. Chainani, M. Matsunami, R. Eguchi, Y. Takata, M. Yabashi, K. Tamasaku, Y. Nishino, T. Ishikawa, S. Tsuda, *et al.*, Physical review letters **104**, 106401 (2010).
[28] F. Lechermann, W. Heckel, O. Kristanovski, and S. Müller, Physical Review B **95**, 195159 (2017).
[29] M. Watanabe, physica status solidi c **6**, 260 (2009).
[30] S. Okamoto and A. J. Millis, Nature **428**, 630 (2004).
[31] K. Szot, M. Rogala, W. Speier, Z. Klusek, A. Besmehn, and R. Waser, Nanotechnology **22**, 254001 (2011).
[32] S. Xue, X. L. Phuah, J. Jian, Q. Li, J. Li, B. Yang, D. Zhang, H. Wang, T. Tsakalakos, A. K. Mukherjee,

et al., Nanoscale **15**, 16752 (2023).